Chapter 2

Mechanical Properties and Microstructure Development in Ultrafine-grained Materials Processed by Equal-channel Angular Pressing

Peter Minárik, Tomáš Krajňák, Ondřej Srba, Jakub Čížek, Jenő Gubicza, Milan Dopita, Radomír Kužel and Miloš Janeček

Additional information is available at the end of the chapter

http://dx.doi.org/10.5772/intechopen.68965

Abstract

In this chapter, the detailed characterization of processes of grain fragmentation and refinement resulting from gradual imposition of strain by individual equal-channel angular pressing (ECAP) passes is reported. A great emphasis is placed on the processing of materials with different crystal structure, particularly the face-centred cubic (FCC), the body-centred cubic (BCC) and the hexagonal close-packed (HCP). Advanced techniques of electron microscopy, electron and X-ray diffraction and positron annihilation spectroscopy have been employed to characterize microstructure, texture and defect evolution in the material as a function of strain imposed by ECAP. Microstructure development was correlated with mechanical properties obtained by both mechanical tests and microhardness measurements. Processes controlling the microstructure refinement and texture development were identified and discussed in detail.

Keywords: ECAP, microstructure, crystal structure, mechanical properties, dislocations

1. Introduction

Ultrafine-grained (UFG) materials processed by severe plastic deformation exhibit enhanced mechanical, electrical, corrosion, magnetic and other physical properties [1]. Several techniques of grain refinement imposing severe plastic deformation (SPD) into the material have been developed in the last several decades. Among them, equal-channel angular pressing (ECAP) has been the most widely used. A large variety of materials—pure metals, alloys,

composites, etc.—with different crystal structure have been successfully processed by ECAP. Usually, a bar- or rod-shaped sample is pressed through a channel in a die, which is bent in a sharp angle where the pure shear occurs (see **Figure 1**).

The cross-section of the sample is unchanged after the processing, and therefore it can be repeatedly processed to obtain high degree of strain. Additionally, there is a possibility to activate different slip systems after each pass by rotating the sample along its processing direction. There are four basic processing routes which describe the way of the billet rotation between individual processing passes. Route 'A' corresponds to no billet rotation, while routes 'B_C' and 'B_A' refer to the rotation by 90° in the same direction and alternate direction, respectively, and route 'C' refers to the rotation by 180° after each pass [3]. The attractiveness of ECAP increases its scalability, which enables the processing of both very small and large samples. Homogeneity of the microstructure is not affected by the size of the sample, and therefore ECAP is a unique technique, which enables production of larger bulk UFG material,

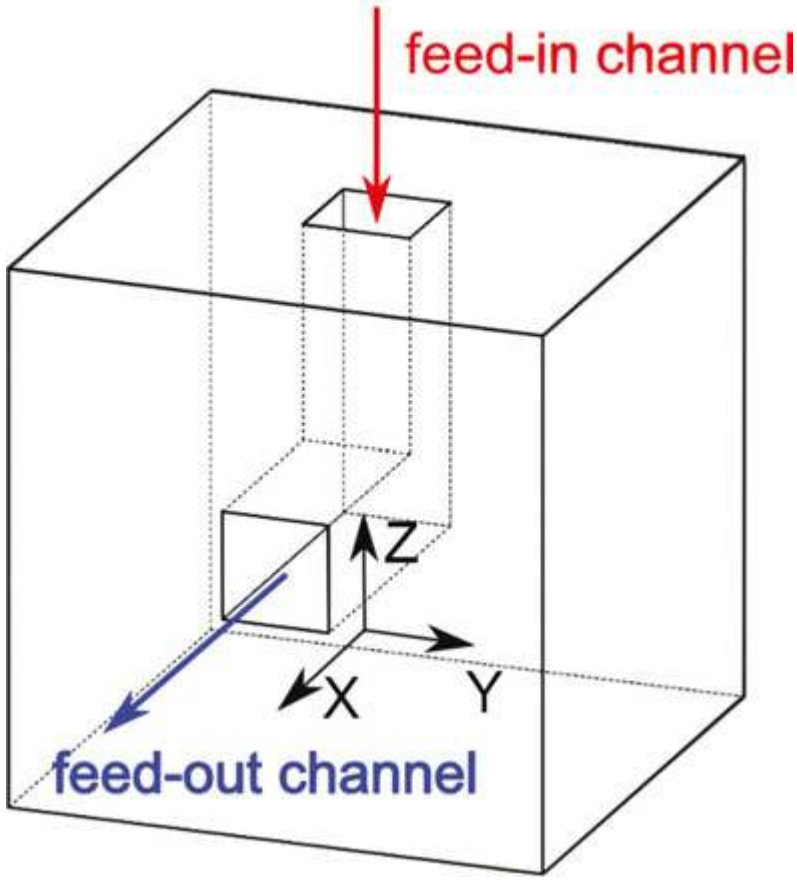

Figure 1. The scheme of the ECAP die including the coordinate system [2].

http://dx.doi.org/10.5772/intechopen.68965

when compared to other SPD techniques. Additionally, continual ECAP, denoted as ECAP-conform, has been developed to process very long sheets and wires [4].

2. Experimental techniques

In this section, the experimental techniques which were employed to characterize microstructure and crystal lattice defect evolution and mechanical properties of the ultrafine-grained materials after ECAP are introduced.

X-ray diffraction line profile analysis (XLPA) and positron annihilation spectroscopy (PAS) are indirect, non-destructive but powerful methods for the characterization of defect structure of ultrafine-grained materials and nanomaterials. The PAS technique is based on the measurement of lifetimes of positrons in irradiated material where the positrons are trapped preferentially on defects of the crystal lattice with lower electron density, which increases effectively their lifetime, with respect to that of free positrons. Detailed information about the principle of PAS is presented elsewhere [5]. The concentration of defects was calculated from PAS parameters using a diffusion trapping model (DTM), assuming non-uniform spatial distribution of defects (dislocations, vacancies, vacancy clusters, etc.) [6, 7]. In this model, the sample is considered as a combination of almost dislocation-free cells having a diameter (d) and dislocation walls containing extremely high dislocation density. The mean dislocation density (ρ) is calculated from the volume fraction of dislocation walls (η), and the dislocation density in the dislocation walls ($\rho_{D,wall}$).

In XLPA technique, the defect structure parameters are derived from the analysis of the width and shape profiles of diffraction peaks. The line broadening due to the strain induced by dislocations and the crystallite size are different in nature, allowing separation of their contributions easily. The results presented in this chapter were obtained from the evolution of high-resolution X-ray diffraction patterns by the convolutional multiple whole profile (CMWP) fitting method [8]. This procedure is based on fitting of the diffraction pattern by the convolution of the background spline, the instrumental pattern and theoretical line profiles reflecting the real structure (crystallite size and dislocations). The theoretical size profile function is modelled by the microstructure consisting of spherical crystallites and the log-normal distribution. The dislocation distribution in individual slip systems is determined by comparison of experimental contrast factors of dislocations and the theoretical values employing the procedure described in detail elsewhere [9].

PAS and XLPA spectroscopic techniques were complemented by direct observations of UFG structure by means of electron microscopy and electron diffraction. Diffraction contrast in the transmission electron microscope (TEM) was employed for the observation of dislocation and subgrain structure [10]. Crystal orientation maps were obtained by electron backscatter diffraction (EBSD) [11]. Measured EBSD data were evaluated by software TSL OIM Analysis 7, which enables to determine the crystallographic microtexture, the character and the fraction of grain boundaries and to evaluate the mean grain size. The macrotexture measurements were performed by X-ray diffraction.

Mechanical behaviour of the samples was tested both under the uniaxial tension with a constant strain rate and by Vickers microhardness measurement, which simulates multiaxial loading.

3. Materials with FCC structure

3.1. Material processing and experimental procedure

Copper of technical purity having the following content of alloying elements (Fe, 0.0037, $P < 0.001$; Sb < 0.0003; Bi < 0.0001; As < 0.001, in wt%) as a typical representative of the material with FCC structure was used in this study. The material received initially as cast condition underwent the homogenization annealing at 450°C for 4 hours. A series of billets of the diameter of 10 × 10 mm and the length of 80 mm were processed by ECAP at room temperature for different numbers of passes N (N = 1, 2, 4 and 8) following route B_C.

Microstructure evolution with strain imposed on the material by different numbers of ECAP passes was investigated by electron microscopy, including EBSD and X-ray diffraction. The evolution of lattice defects (dislocations and vacancies) was investigated by XRD and positron annihilation spectroscopy. Microstructure development was correlated with mechanical properties obtained by tensile tests at room temperature.

3.2. Microstructure evolution

The microstructure of the material in the initial condition is shown in **Figure 2**. It consists of fully recrystallized grains of the average size of approximately 50–100 μm. Numerous twins resulting from the homogenization annealing are also seen at the light micrograph in **Figure 2**.

The microstructure evolution of Cu after different numbers of passes was observed by transmission electron microscopy (TEM). TEM specimens were prepared from the plane perpendicular to the pressing direction (plane X [12]). TEM micrographs displaying the characteristic structures after the individual number of passes are shown in **Figure 3**. It is seen that already after the first ECAP, the strong grain refinement occurs. The microstructure consists of elongated dislocation cells and/or subgrains. Two typical kinds of contrast may be distinguished at the micrograph, namely, dark lines corresponding to dense dislocation walls [13] and bright wider zones comprising individual subgrain boundaries. The comparison of diffraction pattern from both parts of grain boundaries indicates that the majority of grain boundaries have a low misorientation which is characteristic for so-called low-angle grain boundaries (LAGBs). The clear alignment of the structure along <111> direction is seen in the micrograph in **Figure 3(a)**. The overall character of the microstructure corresponds to the heavily deformed material. After the second pass of ECAP (**Figure 3b**), the microstructure remained almost unchanged. The cell/subgrain size was reduced only slightly (the average length of 800 nm and the average width of 200–300 nm) and structure remained aligned along <111> direction. A slight deviation of several subgrains from <111> indicates the activation of other slip systems during the second ECAP pass. After four passes of ECAP, significant

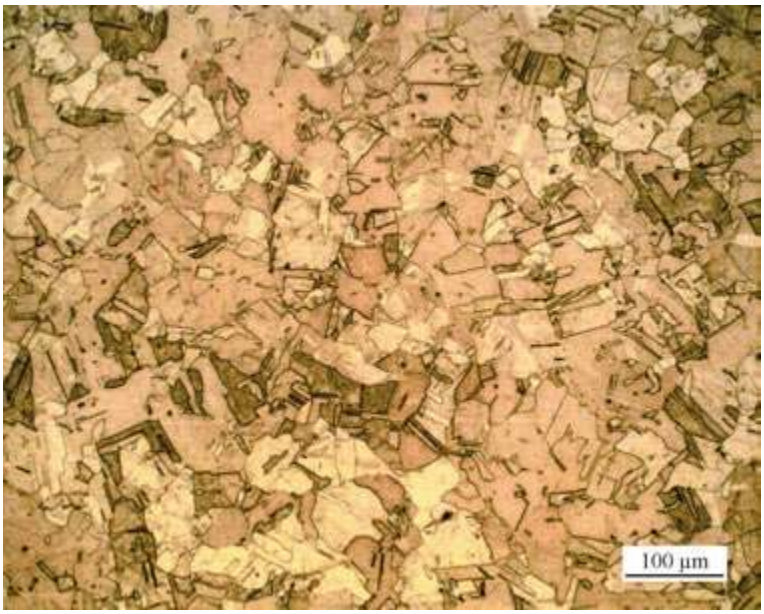

Figure 2. Microstructure of the non-deformed Cu.

changes in the microstructure occurred (see **Figure 3c**). The majority of grains are already equiaxed and the fraction of high-angle grain boundaries (HAGBs) characterized by typical thickness fringes contrast increased. The activation of new glide systems in planes which are not parallel with the original glide planes due to the rotation of the billet between individual passes must have occurred between the second and fourth pass. The typical microstructure of the specimen after eight passes is shown in **Figure 3(d)**. The microstructure is homogeneous consisting of equiaxed grains separated by sharp HAGBs. Significantly lower density of dislocations in grain interiors was observed in this condition. The average grain size ranged between 200 and 300 nm. In some zones, subgrains/grains with as large as about 500 nm were also observed. TEM observations confirm the efficient grain refinement of Cu polycrystals by ECAP (factor of 1000).

Inverse pole figures obtained from *EBSD measurements* are presented in **Figure 4**. The results are consistent with local TEM observations. Relatively large areas of boundaries with low misorientations indicated by slight colour code variations corresponding to bands subgrains observed by TEM (cf. **Figure 2**) dominate the microstructure [14]. With increasing the number of ECAP passes, much smaller subgrains and grains having larger misorientations evolve from these zones. A detailed analysis of grain boundary character distributions in individual specimens after ECAP is given elsewhere [15]. In specimens after four and eight passes, EBSD measurements revealed a high density of twin ($\sum 3$) and multiple twin boundaries $\sum 3^n$ ($\sum 9$, $\sum 27$), see **Figure 5**. Other authors also reported a similar result. This extensive formation of $\sum 3^n$ special boundaries is assumed to occur only after extensive strain hardening imposed by severe plastic deformation once a certain critical dislocation density

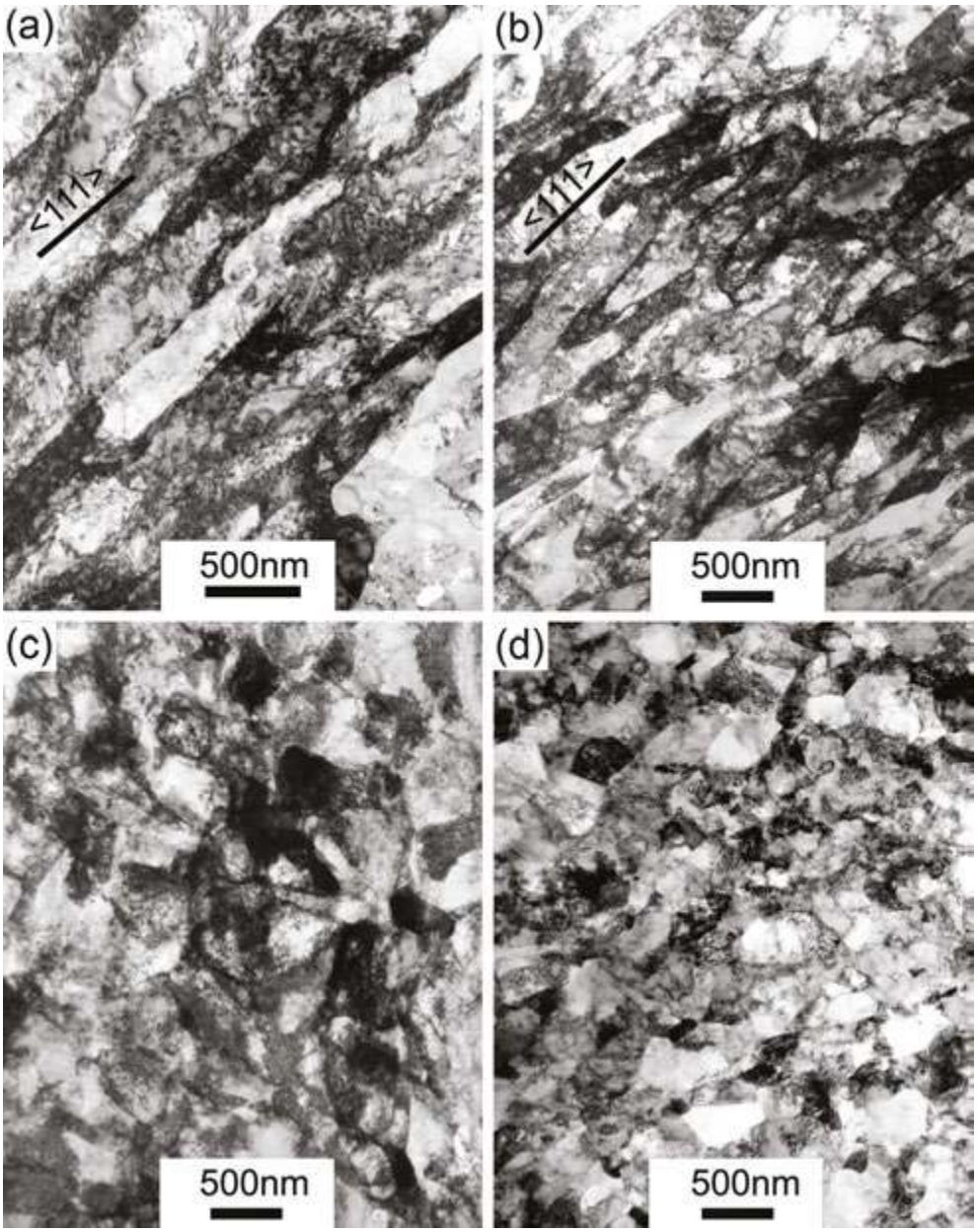

Figure 3. TEM micrographs of the typical microstructure of Cu specimens after different number of ECAP passes N (plane X) (a) $N = 1$, (b) $N = 2$, (c) $N = 4$ and (d) $N = 8$.

http://dx.doi.org/10.5772/intechopen.68965

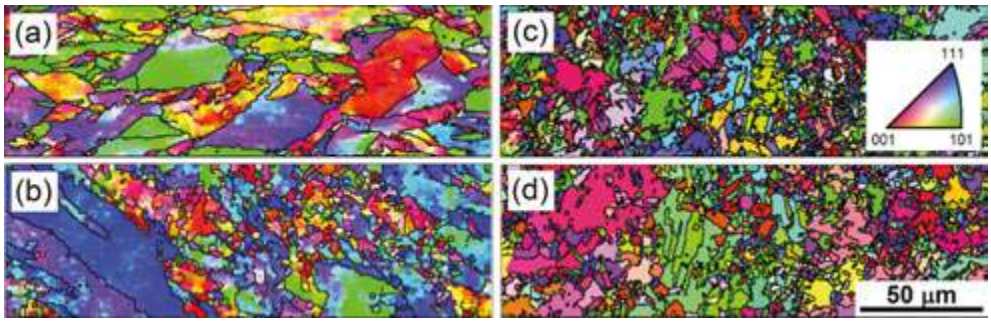

Figure 4. IPF map of ECAP specimens (a) 1P, (b) 2P, (c) 4P, (d) 8P (plane X).

is reached [16, 17]. EBSD also confirmed enhanced presence of LAGBs in the specimen after 1P (see **Figure 5**). With increasing strain due to ECAP, LAGBs ($\theta < 15°$) were continuously transformed into HAGBs ($\theta > 15°$). After eight passes, almost 90% of all grain boundaries had a high-angle character as displayed in **Figure 6**.

It is well known that the material subjected to severe plastic deformation contains high density of lattice defects, namely, dislocations and point defect. The evolution of density of lattice defects as a function of the number of ECAP passes was investigated by *positron*

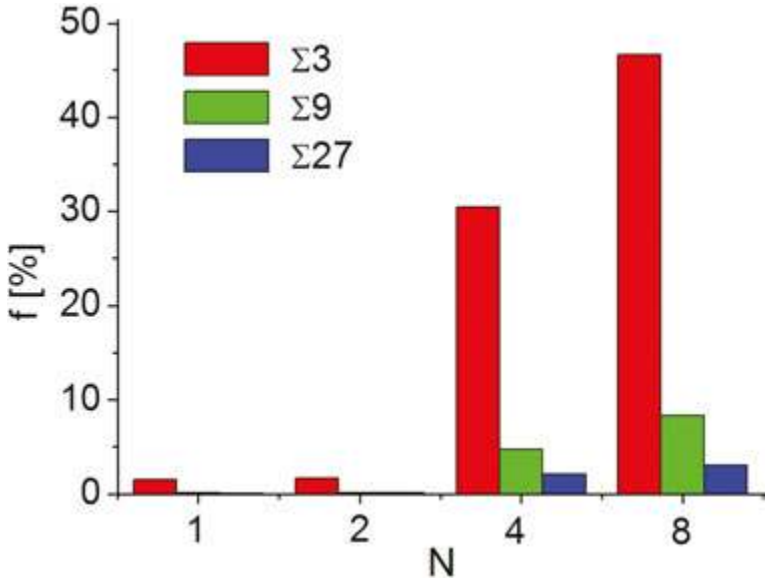

Figure 5. Special boundaries distribution.

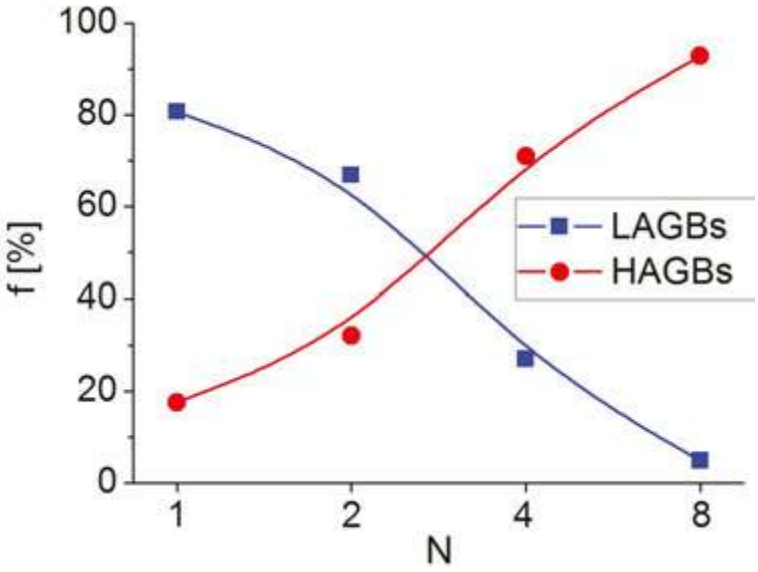

Figure 6. GB character evolution in ECAP Cu.

annihilation spectroscopy. Three different components were found in positron lifetime (PL) spectra as depicted in **Figure 7(a)**: (i) a component corresponding to free positrons which are delocalized in the lattice with the respective lifetime $\tau_1 \approx 114$ ps and the relative intensity I_1, (ii) a component representing the contribution of positrons trapped at dislocations [18] having a lifetime of $\tau_2 \approx 164$ ps and the intensity I_2, and (iii) a component attributed to positrons trapped at small vacancy clusters called microvoids formed by clustering of vacancies generated by ECAP [7] with the lifetime τ_3 depending on the number of vacancies in the cluster and the intensity I_3.

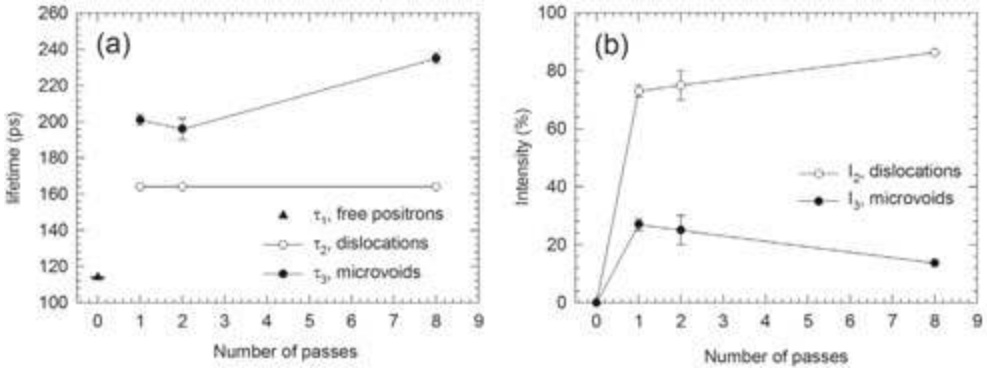

Figure 7. PAS results for Cu specimens subjected to various numbers of ECAP passes: (a) lifetimes of the components resolved in PL spectra, (b) intensities of the components arising from positrons trapped at defects.

http://dx.doi.org/10.5772/intechopen.68965

In annealed non-deformed Cu specimen ($N = 0$), only a single component PL spectrum having a lifetime of $\tau_1 = 114$ ps, $I_1 = 100\%$, was found (cf. **Figure 7a**). In this specimen, all positrons are annihilated from the free state. It should be noted that the lifetime τ_1 agrees well with the theoretically calculated lifetime of free positrons in Cu [19].

In all specimens deformed by ECAP, no free positron component was found $I_1 = 0\%$ (so-called saturated trapping). The evolution of lifetimes with N indicates that the component τ_2 is independent of N testifying that only the density of dislocations changes during ECAP pressing while the character of dislocation traps does not. On the other hand, the component τ_3 changes with increasing number of passes corresponding to the change of the microvoid size, i.e. the number of vacancies in the respective microvoids.

Due to the high density of lattice defects in ECAPed Cu specimens, almost all positrons are trapped at the open volume around these defects. In this case, the dislocation density ρ_D exceeds the value of 10^{14} m^{-2} and the microvoid concentration c_v the value of 10^{-4} at^{-1}. The intensity of positrons trapped at dislocations $I_2$was found to increase with increasing number of ECAP passes as shown in **Figure 7(b)**. On the other hand, the intensity of positrons trapped at microvoids I_3increases only during the first pass, while for $N > 1$ it decreases continuously up to $N = 8$.

Due to the saturated trapping of positrons in defects ($I_1 = 0\%$), it is not possible to determine the absolute values of defect densities from the DTM model [5, 7]. Instead of that, only the ratio of the respective defect densities (ρ_D/c_v) may be determined from the ratio of respective intensities of positrons trapped at dislocations and at microvoids I_2/I_3 according to the formula (1) [7], where K_D and K_v are the trapping rates of positrons to dislocations and to microvoids, respectively. The variation of the ratio K_D/K_v with the number of ECAP passes is plotted in **Figure 8(a)**. The curve indicates that the dislocation density increases faster than the concentration of microvoids in all specimens deformed by ECAP.

$$\frac{I_2}{I_3} = \frac{K_D}{K_v} \sim \frac{\rho_D}{c_v} \tag{1}$$

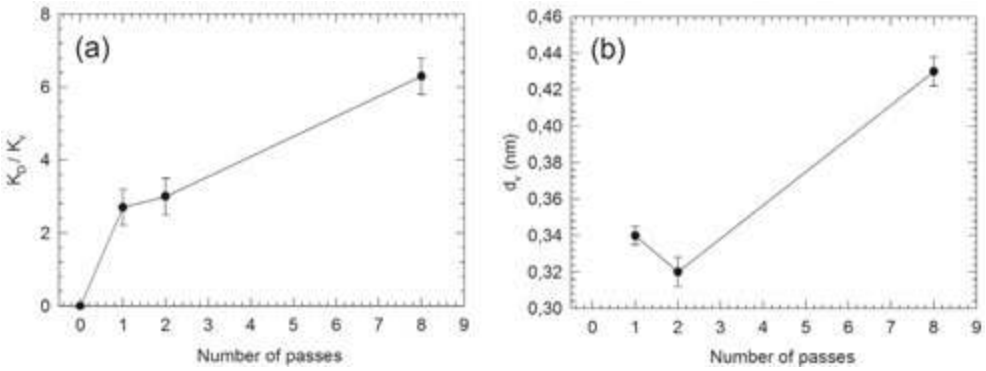

Figure 8. (a) The ratio K_D/K_v of positron trapping rate to dislocations and microvoids, (b) diameter of microvoids calculated from PAS results.

Theoretical calculations described in detail in Ref. [7] allow one to determine qualitatively the size of microvoids from the component $\tau_{3.}$ **Figure 7(b)**, which presents the dependence of the microvoid diameter d_v as a function of the number of passes, shows the results of these calculations. The microvoid diameter size change seems to be statistically insignificant in specimens deformed up to $N = 2$, while significantly larger microvoids (containing the higher number of monovacancies) are created in specimens deformed by eight ECAP passes.

The drawback of the PAS, which is unable to determine quantitatively the dislocation density in specimens containing high density of these defects ($\rho \geq 10^{14}$ m^{-2}, saturated trapping) [4, 6] is smeared by employing other technique, namely, *X-ray diffraction* (XRD), making use of the fact that peak broadening is caused both by the size of coherently scattering domains and by the presence of strain in the material. The former effect allows determining the size of these domains while the latter one allows to determine quantitatively the density of dislocation employing the techniques of the whole total patter fitting considering the size and dislocation broadening models proposed by Ribárik et al. [20] and Matěj et al. [21]. Extended FOX model proposed by Matěj et al. [21] was used to evaluate the results of XRD measurements in Cu specimens deformed by ECAP. This model uses 4 to 5 fitting parameters, namely, the dislocation density, the mean crystallite size, the dislocation correlation factor, the variance of the size distribution and/or the fraction of screw and edge dislocations, respectively. The details of fitting procedure are described in detail elsewhere [20]. The results of the fitting procedure are summarized in **Table 1**.

The density of dislocations ρ_D was found to increase with increasing number of ECAP passes which is in good agreement with qualitative predictions of PAS. Moreover, the fraction of edge dislocation decreases with increasing strain, which is consistent with results of other authors obtained on Cu [22]. This fact is attributed to the enhanced mobility of edge dislocations compared to screw ones [23]. The mean crystallite size determined by XRD is significantly lower than that obtained by TEM or EBSD. It is well known that crystallite size determined by XRD corresponds to the size of coherently scattering domains which reflects the size of subgrains rather than grains [24]. As a consequence, the values of <*L*> are significantly lower than the values of grain size determined by electron microscopy and electron diffraction <d> (see **Table 1**).

3.3. Mechanical properties

Mechanical properties were determined by testing tensile specimens in a universal screw-driven Instron 5882 machine at the initial strain rate of 4×10^{-4} s^{-1}at room temperature (RT).

Sample	ρ_D, 10^{15} m^{-2}	w	<L>, nm	<d>, nm
$N = 1$	2.1	0.95	78	900–700
$N = 2$	6.6	0.85	71	800–700
$N = 8$	7.9	0.35	76	150–250

Note: ρ_D—dislocation density; w—fractions of edge dislocations; <*L*>—the mean crystallite size;**<d>** , nm—the grain size determined by TEM/EBSD.

Table 1. Structure parameters for ECAP Cu samples for different numbers of passes $N = 1$, 2 and 8.

http://dx.doi.org/10.5772/intechopen.68965

The true stress-true strain curves for the non-deformed (0P) and ECAPed specimens (N = 1, 2, 4 and 8P) are shown in **Figure 9**. **Table 2** summarizes tensile test data in terms of the yield $\sigma_{0.2}$ and ultimate tensile strength σ_{max}(YS and UTS, respectively) and the total elongation (ε_{tot}).

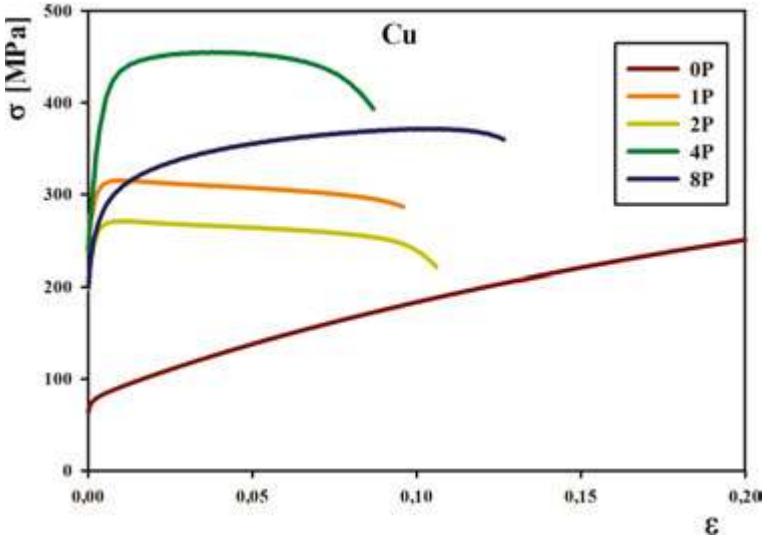

Figure 9. True stress vs. true strain curves of Cu specimens after different numbers of ECAP passes.

ECAPed specimens exhibit significantly better mechanical properties as compared to the coarse-grained material (N–0). Both YS and UTS increase up to four ECAP passes and slightly decline after eight passes. Mechanical properties correlate well with the microstructure evolution in individual specimens after ECAP. The increase of both YS and UTS up to four passes corresponds well to the combined effect of both the reduction in grain size and the increase of dislocation density. As no significant change of grain size was found in specimens $N > 4$, the mechanical properties in these specimens are influenced mainly by dislocation density variations. PAS (qualitatively) and XRD (quantitatively) measurements indicate that ρ_D increases up to $N = 4$ and is followed by a slight decline in the specimen $N = 8$ [25]. It is fully consistent with the evolution of mechanical properties with strain imposed by ECAP. However, the drop of YS and UTS in the specimen after

No. of passes/*N*	**0**	**1**	**2**	**4**	**8**
$\sigma_{0.2}$ (MPa)	78	293	250	330	258
σ_{max} (MPa)	215	314	270	455	371
ε_{tot} (%)	40	9.5	10.6	8.7	12.7

Table 2. Summary of experimental data obtained from mechanical testing.

eight passes may also be attributed to other microstructural effects, in particular the development of the grain boundary character distribution (cf. **Figures 4** and **5**) and the texture development which is currently under evaluation.

4. Materials with BCC structure

4.1. Material processing and experimental procedure

Single-phase ferritic interstitial-free (IF) steel having the BCC crystal structure and the carbon content less than 0.01 wt% was pressed through a rectangular ECAP die at room temperature (RT). ECAP billets were pressed for one, two, four and eight passes with the speed of 2 mm/min via route B_C. Microstructural characterization of samples was performed by conventional EBSD and TEM techniques. The lattice defects were studied by positron annihilation spectroscopy (PAS) employing the diffusion trapping model (DTM) [6, 7]. Mechanical properties at RT were characterized by Vickers microhardness measurement and the tensile tests with a constant strain rate of 10^{-3} s^{-1}. Detailed information about the composition, sample preparation and experimental methods can be found elsewhere [26–28].

4.2. Microstructure characterization by EBSD and TEM

Figure 10 shows the homogeneous microstructure of the initial state. The high-angle grain boundaries (HAGBs) (>15°) are outlined by black colour. The microstructure exhibits random crystallographic texture and is formed by equiaxed grains with a mean grain size of about 41 μm. The mean grain size was determined from the EBSD images as the area-weighted mean grain size and only grains separated by HAGBs were taken into account. Microstructural evolution during ECAP processing is displayed in **Figure 11**. Increasing the number of ECAP passes (*N*) leads to the gradual refinement of the microstructure. After the single ECAP pass, heavily deformed grains can be observed. Different colour inside the original grains indicates the formation of subgrains or dislocation cells having low-angle misorientations (LAGBs). After the second pass, the misorientation across the low-angle grain boundaries increases and some of them are transformed into the high-angle grain boundaries indicated by the black colour. With further straining, the gradual increase in the fraction of HAGBs can be observed. After 8 passes, almost fully refined microstructure with the average grain size of 0.7 μm and the fraction of HAGBs 65% was observed.

Detailed TEM observation confirmed the formation of bands of subgrains with sharp boundaries and dislocations cells with fuzzy boundaries in the sample after the single pass (see **Figure 12a**). After eight passes, new refined grains with the size around 500 nm are formed from subgrains in these deformation bands. As a consequence, the misorientation of refined grains remains low in same regions, i.e. they are separated predominantly by LAGBs. Additionally, a non-uniform spatial distribution of dislocations was observed: grain/subgrain interiors almost free of dislocations are separated by distorted layers with a very high density of dislocations. Mechanism of grain refinement described above was observed in many other materials with FCC and BCC crystal structure processed by ECAP [29–32].

http://dx.doi.org/10.5772/intechopen.68965

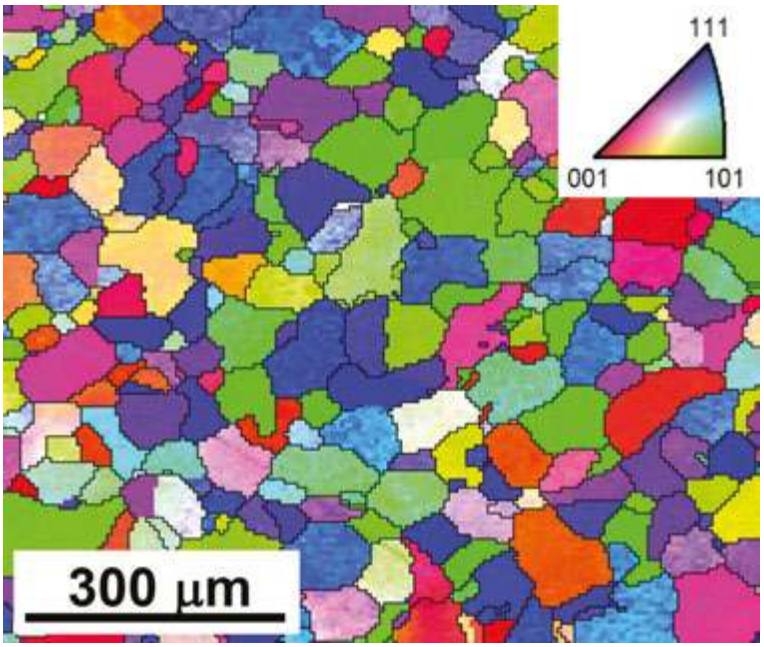

Figure 10. EBSD inverse pole figure map of the initial state (size-rolled and homogenized for 1 hour at 700°C).

Microtexture evolution during ECAP processing is described by a series of EBSD (100) and (110) pole figures measured on the plane X [12], lying perpendicular to the pressing direction (see **Figure 13**). With increasing number of passes, a gradual formation of three strong maxima in the EBSD (110) pole figure was observed. The maxima are tilted by 45° from each other. The analysis of interplanar angles in cubic crystals [33] indicates that these maxima are associated with {110} planes. After the eight passes, the stronger (110) texture in comparison with that after four passes is formed. This is consistent with the observations of De Messemaeker et al. [34]. The maxima are tilted roughly by 20° towards the y-axis. This is consistent with the cloud-model of Toth and co-workers [35, 36] and has been reported by other authors in BCC material [35–37].

4.3. Defect structure investigation by PAS

Lifetimes of the exponential components resolved in the lifetime (LT) spectra are plotted in **Figure 14(a)** as a function of the number of ECAP passes. The initial sample (0N) exhibits a single component spectrum with the lifetime of ≈108 ps, which can be attributed to the positrons annihilated in the free state. As a consequence, the initial sample exhibits a low density of defects (dislocation density below 5×10^{12} m^{-2}). The samples deformed by ECAP ($N > 0$) exhibit two-component LT spectra. Apart from the component τ_1 attributed to positrons not trapped at defects, the longer component with the lifetime $\tau_2 \approx 150$ ps coming from positrons trapped at dislocations [38–40] were detected in specimens $N > 0$. Park et al. [38] performed a

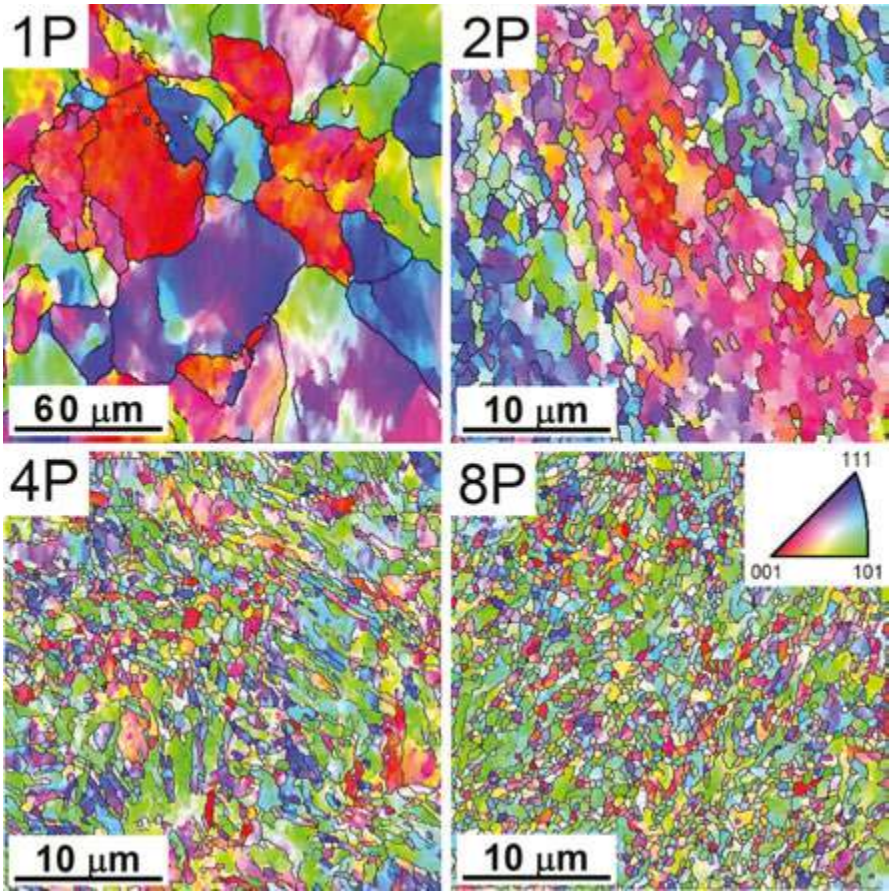

Figure 11. EBSD inverse pole figure maps obtained on the cross-sections of the samples processed by ECAP for different numbers of passes.

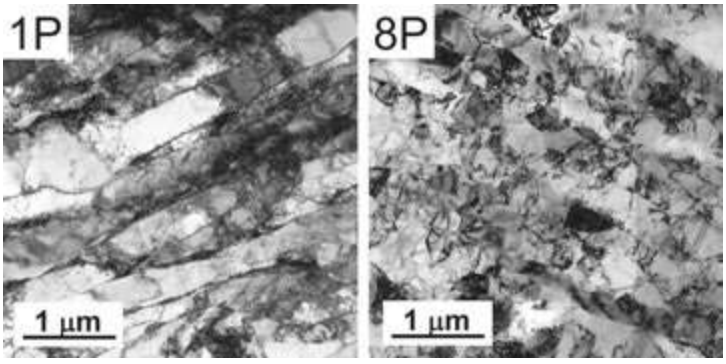

Figure 12. A bright-field TEM micrographs of IF steel samples deformed by applying (a) 1 pass and (b) 8 passes.

http://dx.doi.org/10.5772/intechopen.68965

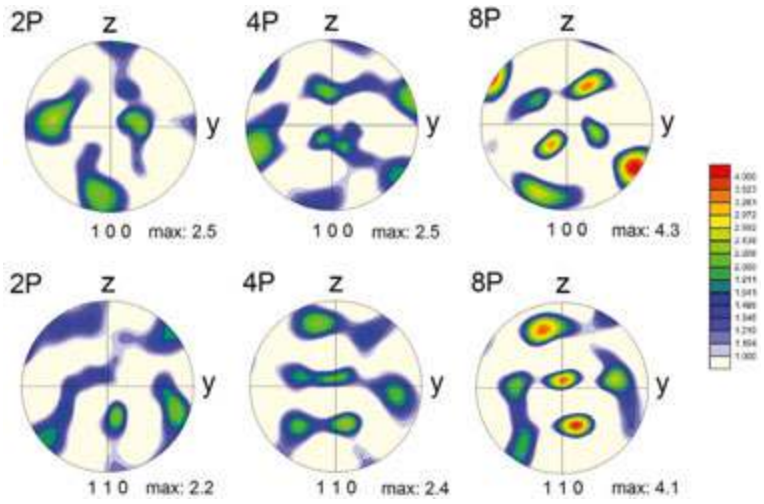

Figure 13. EBSD (100) and (110) pole figures for the IF steel samples processed by ECAP for different numbers of passes.

detailed LT investigation of deformed Fe and reported that the lifetimes of positrons trapped at edge and screw dislocations are τ_{edge} = 165 ps and τ_{screw} = 142 ps, respectively. As a consequence, the lifetime $\tau_2 \approx 150$ ps determined in IF steel deformed by ECAP can be attributed to positrons trapped at a mixture of edge and screw dislocations. The fraction of screw dislocations f_{screw} was determined from the lifetime τ_2 according to the relation:

$$f_{screw} \approx \frac{\tau_{edge} - \tau_2}{\tau_{edge} - \tau_{screw}} \tag{2}$$

The IF steel contains $f_{screw} \approx 0.7$ after the first ECAP pass. During further ECAP processing, the screw/edge character of dislocations remains almost unchanged, as indicated by almost constant value of the lifetime τ_2 in **Figure 14(a)**. More screw character of dislocations was also observed in ECAP deformed Cu as reported in Section 3.2. In BCC lattice of IF steel, the screw dislocation core is dissociated into a non-planar configuration [41]. As a consequence, during

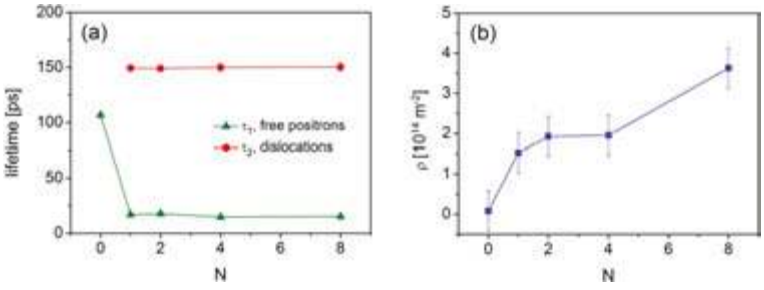

Figure 14. Development of (a) lifetimes of the components resolved in LT spectra and (b) the mean density of dislocations ρ determined by PAS with increasing number of ECAP passes. The initial sample before ECAP processing is labelled as 0N.

ECAP pressing, edge dislocation segments annihilate more easily than the screw ones and the remaining dislocations have therefore a more screw character. The development of the mean dislocation density (ρ) determined from LT data applying the DTM is plotted as a function of N in **Figure 14(b)**. The mean dislocation density gradually increases with increasing number of ECAP passes and saturates at $\approx 4 \times 10^{14}$ m^{-2}.

4.4. Mechanical properties

The results of mechanical testing at RT showed that ECAP processing significantly influences the mechanical properties of IF steel (see **Figure 15**). The values of microhardness (HV) and tensile strength (σ_{max}) gradually increase with increasing N and are the same within the experimental error (see **Figure 15a**). Assuming that microhardness test introduces the multiaxial loading to the material in comparison to the uniaxial tensile test, the consistency in the values of HV and σ_{max} indicates a negligible effect of the texture on the mechanical properties. On the other hand, the yield stress ($\sigma_{0.2}$) significantly increases already after a single pass as a result of the rapid increase of dislocation density and simultaneous grain refinement. Further straining leads to the only moderate increase of $\sigma_{0.2}$due to the slight increase of dislocation density and continuous grain refinement. A similar behaviour was observed in ECAP-processed aluminium alloy 6016 [42]. The overall increase in the tensile strength and the yield stress was about 230 and 450%, respectively. As it is apparent from **Figure 15(b)**, increasing strength of the samples is accompanied by a rapid decrease of ductility, which drops from 45% for initial sample to approximately 10% after eight passes. Such reduction in the ductility is typical for ECAP-processed materials and can be explained by reducing mobility of dislocations due to the considerable increase of dislocation density [43, 44]. It can be concluded that mechanical properties of ECAP processed IF steel are controlled mostly by grain size and dislocation density.

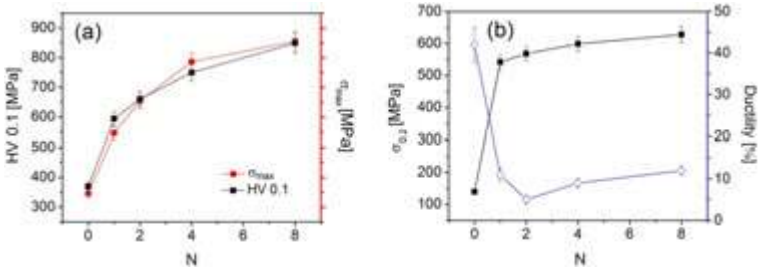

Figure 15. Development of (a) microhardness, tensile strength and (b) yield stress, ductility of IF steel with increasing numbers of ECAP passes.

5. Materials with HCP structure

Since the first introduction of ECAP, magnesium is the most intensively investigated HCP metal. Its processing is much more difficult than the processing of FCC and BCC metals, because of the limited number of available slip systems in the HCP structure at RT. Therefore,

much higher processing temperature is often needed, which significantly complicates achieving average grain size below 1 μm because of grain growth at elevated temperatures. Nevertheless, the improvement in the processing technique, especially by the utilization of back pressure in the exit channel enables to decrease the processing temperature and finally to achieve much finer microstructure. In this section, the effect of the processing parameters and the composition of the alloy on the microstructure development and resulting mechanical properties in magnesium alloys are introduced and discussed.

The most important parameters that could be varied in ECAP processing are the processing temperature and the processing route. Both parameters have significant influence on the resulting microstructure, and consequently on physical properties of the final material. The processing temperature is an experimental parameter and needs to be optimized for each alloy separately. The processing temperature is usually around 200°C, but for certain alloys, particularly those with the high content of rare earth elements, the processing temperature up to 350°C needs to be used. In the next paragraphs, the effect of processing route and processing temperature selection on the example of a commercial AX41 (Mg, 4 wt%; Al, 1 wt% Ca) magnesium alloy is analysed.

5.1. Effect of the processing route

The microstructure of the extruded (EX) sample is shown in **Figure 16**. Homogeneous distribution of equiaxed grains with an average grain size of 10 μm was observed in both section planes. Texture of the extruded sample was typical for most magnesium alloys, namely, $\langle 10\bar{1}0 \rangle$ fibre texture with a fibre parallel to the extrusion direction (see **Figure 17**).

The extruded samples were subsequently processed by ECAP following three different processing routes—A, B_C and C. Eight passes through ECAP resulted in gradual refinement of the microstructure. Microstructure of specimens processed by 8P irrespective of the processing route is shown in **Figure 18(a–c)**. Nevertheless, the fragmentation rate and the final grain size depend strongly on the individual ECAP routes. The evolution of the average grain size for all samples/routes is shown in **Figure 18(d)**. The mean grain size was determined from the EBSD images as the area-weighted mean grain size. From the results, it may be concluded that the routes C and B_C were more effective during the first steps of the processing and homogeneous

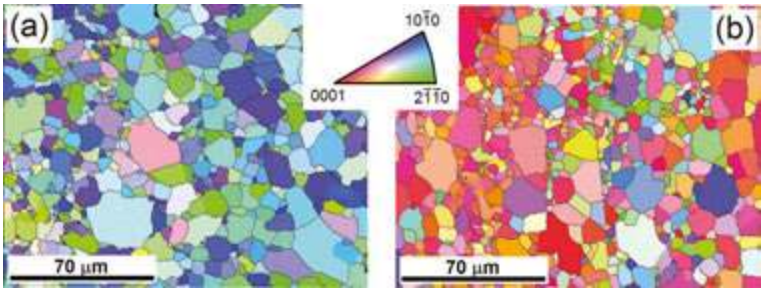

Figure 16. EBSD inverse pole figure maps obtained on the (a) cross-section and (b) longitudinal section of the extruded sample.

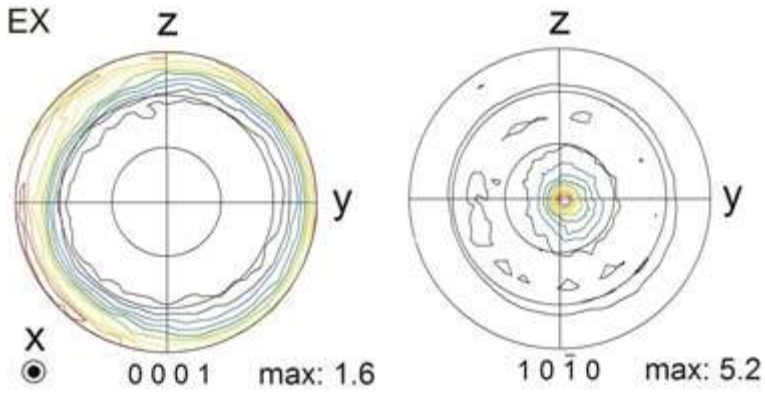

Figure 17. (0001) and (10$\bar{1}$0) X-ray pole figure measured on cross-section.

fine-grained microstructure was attained already after four passes (see Ref. [45]). The average grain size of samples processed via route B_C was unchanged during subsequent passes, but extensive grain growth was observed in samples processed via route C. The resulting value of average grin size was ~2.7 μm for route B_C and ~4.5 μm for route C. In the case of route A, the grain refinement was continuous and homogeneous microstructure was attained only after eight passes through ECAP, with the average grain size of ~2 μm.

The grain refinement during ECAP is based on two mechanisms that are working cooperatively. The first one is a nucleation and growth of fine grains along former grain boundaries and the second one is the formation of high-angle grain boundaries from dislocation tangles [46]. The first one is a more intensive refinement process in HCP structures, whereas as mentioned earlier, the second one is more intensive in FCC and BCC structures. These two mechanisms usually lead to gradual grain refinement until grain growth and grain refinement are in balance, as it was observed in the case of route B_C after 4P. Nevertheless, a different evolution of the structure and grain refinement was observed for samples processed via routes A and C. This difference could be explained by the analysis of the Burges vectors population in the individual samples. The analysis of the distribution of dislocations in the non-basal <a> slip systems, which was performed using the procedure described in detail in [9], is shown in **Figure 19**. Prismatic and pyramidal (PrE + PyE) <a>-type dislocations evolution as a function of the number of ECAP passes for different processing routes, are shown together because of the analysis limitation. The complete analysis of all major slip systems is described in detail elsewhere [45]. The significant dislocation activity observed in all samples/routes is consistent with theoretical calculations [47, 48], where modelling results indicating that approximately 20% of strain accommodated by prismatic <a>-slip are presented. The non-basal <a>-dislocations are very important for grain refinement, because they have the high probability to lock each other and form dislocation tangles even in small grains. Therefore, substantially higher fraction of these dislocations in samples processed via route A are responsible for higher grain refinement and vice versa, i.e. the reduction of non-basal <a>-dislocations fraction in samples processed via route C resulted in grain growth. The activity of a particular slip system is highly dependent on the grain orientation and therefore on the texture of the material.

http://dx.doi.org/10.5772/intechopen.68965

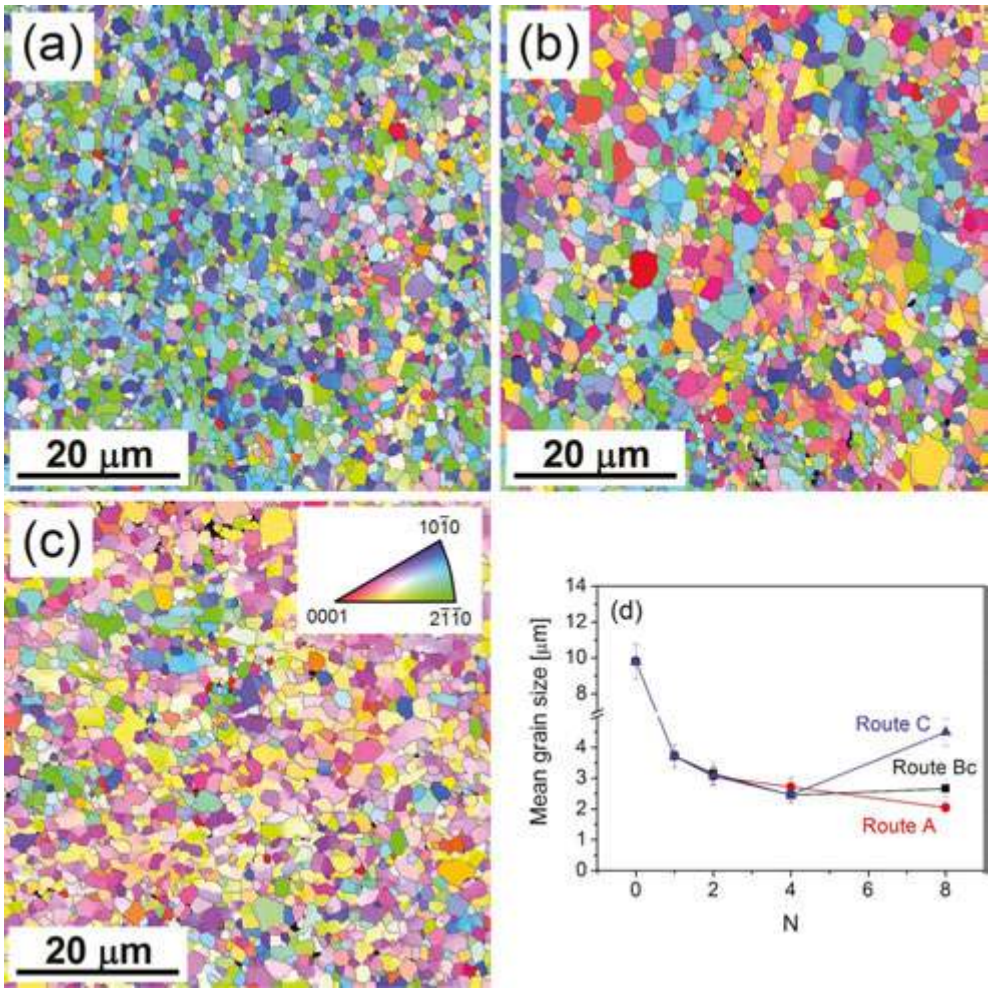

Figure 18. EBSD inverse pole figure maps obtained on the samples processed by 8 passes via route (a) A, (b) B_C and (c) C. (d) Evolution of the mean grain size in the samples processed by different routes.

Different processing routes influence significantly the texture development. Therefore, the higher activity of non-basal <a>-dislocations in samples processed via route A than route C is caused by the preferred orientation of individual grains. In **Figure 20**, pole figures measured on the samples after the final stage of the processing (8P) are displayed. Two kinds of texture components could be recognized. The first texture component, denoted as M, represents basal planes normal to the z-direction. The second texture component, denoted as N, represents basal planes lying parallel to the theoretical shearing plane activated during ECAP [49], i.e. the basal planes are tilted by ~45° to the pressing x-direction. The formation and intensity of the particular texture component is strongly influenced by the processing route. Whereas texture component M is dominant in samples processed via route A, it is completely missing in

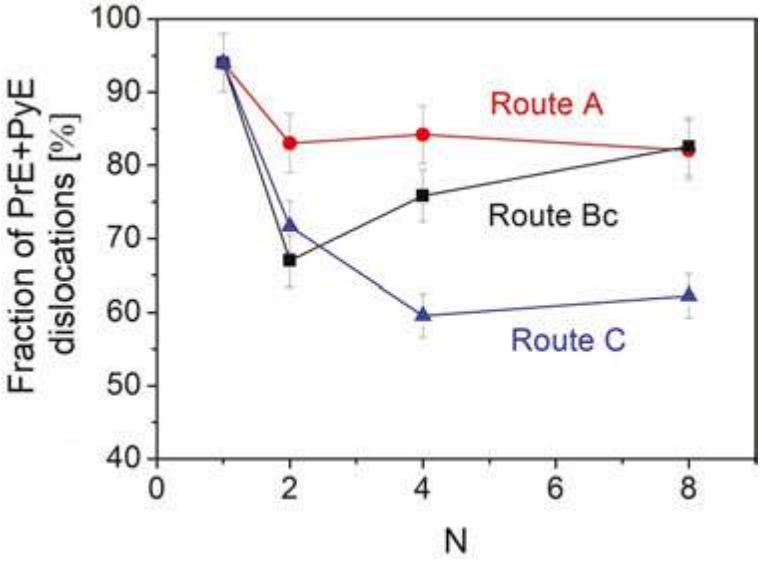

Figure 19. The dependence of the sum of relative fractions of prismatic (PrE) and pyramidal (PyE) <a>-type edge dislocations on the route of ECAP and the number of passes.

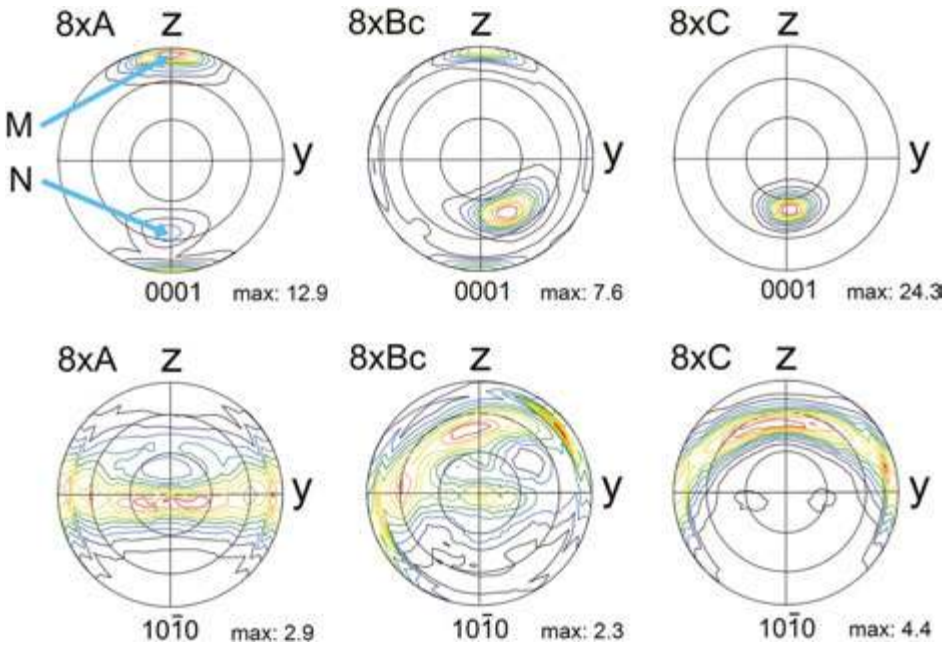

Figure 20. (0001) and (10$\bar{1}$0) X-ray pole figures for the samples processed by different routes.

http://dx.doi.org/10.5772/intechopen.68965

samples processed via route C. Thus, the texture component N is the only component in samples processed via route C. In the sample processed via route A, the component N is strongly suppressed. In the case of the route B_C, the situation is more complicated. The microstructure exhibits both texture components. The dominant texture component is N, which is additionally tilted roughly by 40° towards y-direction. Gradual transformation of the texture components during successive ECAP passes is described in detail elsewhere [45].

The formation mechanisms of these texture components at an expense of the initial fibre texture are the following. The texture component N is formed by predominant activation of the basal slip system during the processing, which causes the rotation of the (0001) basal planes parallel to the theoretical shearing plane (see **Figure 21b**). The formation mechanism of this texture component is discussed in different papers with the same conclusion [49–54]. The origin of the texture component M is the combination of twinning which occurs already in the feed-in channel during pressing and the activation of the second-order pyramidal slip in which the pyramidal plains $\{11\bar{2}2\}$ remain orientated parallel to ECAP shearing plane (see **Figure 21a**). For full description of the formation mechanism of both texture elements, the reader is referred to Refs. [45, 55]. The occurrence of compression twining in the extruded pure magnesium and its alloys was also reported by many authors [56, 57].

The formation of a particular texture component and its strength is given by the route of ECAP processing. Rotation of the sample after the *n*th ECAP pass, which differentiates the type of the route, defines the orientation of the shearing plane towards the pre-existing texture components during the subsequent pass. Processing of the sample without any rotation (route A) causes the generation and strengthening of the texture component M. Reorientation of individual grains towards the M component after each pass results in unfavourable orientation for the basal slip in the subsequent pass. Therefore, this texture component is very weak. Additionally, grains representing the M component are oriented well for twinning in the feed-in channel, and subsequently, the second-order pyramidal slip is activated and strengthens the texture component M, as shown in **Figure 21**.

In the case of route C, the sample is rotated 180° along its processing direction after each pass. Grains representing the texture component N have basal planes aligned with the ECAP

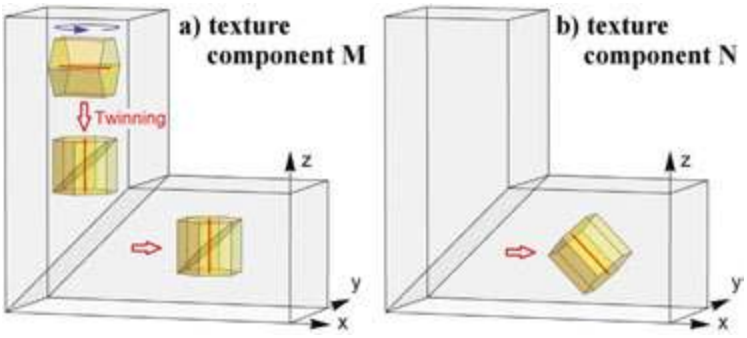

Figure 21. Formation mechanism of the texture components (a) M and (b) N.

shearing plane and therefore there is no rotation of these grains during the subsequent pass. Moreover, the activation of the basal slip in other grains results in strengthening of the component N. The formation of this texture component is very effective, and one can notice that the texture strength in the sample processed via this route is significantly higher than in samples processed via the other routes.

The pole figure of the sample processed by route B_C is a combination of the previous two ones. Rotation of the sample by 90° along the processing direction partially suppresses the strengthening mechanism of the N component. The initial extrusion texture is favourable for the formation of the M component, because the majority of grains are well oriented for twinning in the feed-in channel. However, the fraction of these grains gradually decreases as more grains are reoriented to form the N component. In this orientation, the grains can no longer twin in the feed-in channel and consequently generate the M component. Therefore, in some works describing the evolution of the texture in Mg alloys processed via route B_C, the texture component M is present after the final pass and in some is not. Its presence is given by the effectivity of twinning of the grains in the feed-in channel and the rate by which the texture component N strengthens. This rate is affected particularly by the processing temperature, as discussed below.

5.2. Effect of the processing temperature

The effect of the processing temperature is more straightforward than the effect of the other processing parameters. The higher processing temperature makes usually the processing itself easier while it increases the tendency for the grain growth. Magnesium must be processed at elevated temperatures because of the billet segmentation, which occurs at the lower temperatures [58]. The high limit for the processing temperature fundamentally does not exist, but it is always necessary to process at the lowest possible temperature to obtain the most effective grain refinement. In the previous section, the grain refinement and texture formation for the extruded AX41 processed at 220°C via route B_C were discussed. This temperature was found to be the lowest one for this alloy. In this section, the effect of increase of the processing temperature to 250°C is shown and discussed.

The microstructure of the sample processed at 250°C temperature was comparable to that processed at 220°C. Nevertheless, the apparent negative effect of the increased processing temperature on the grain size is clearly seen in **Figure 22**. At 250°C, the grain refinement was observed only up to two passes. During further straining ($N > 2$), the grain growth occurs. The final average grain size was ~4 μm, while for lower processing temperature (220°C), it was ~2.7 μm only. Another significant effect of the increase of the processing temperature was observed in texture development. In **Figure 23**, pole figures of the 8P sample processed at 250°C are shown. The formation of the texture component M is significantly suppressed at the higher temperature, cf. **Figure 20**. This difference results from the suppression of twinning at elevated temperatures. As a result, after eight passes, the M component is strongly suppressed in specimen deformed at the higher temperature.

5.3. Effect of the composition

The influence of the composition on the deformation behaviour and resulting microstructure evolution in magnesium alloys has been intensively studied for a variety of processing

http://dx.doi.org/10.5772/intechopen.68965

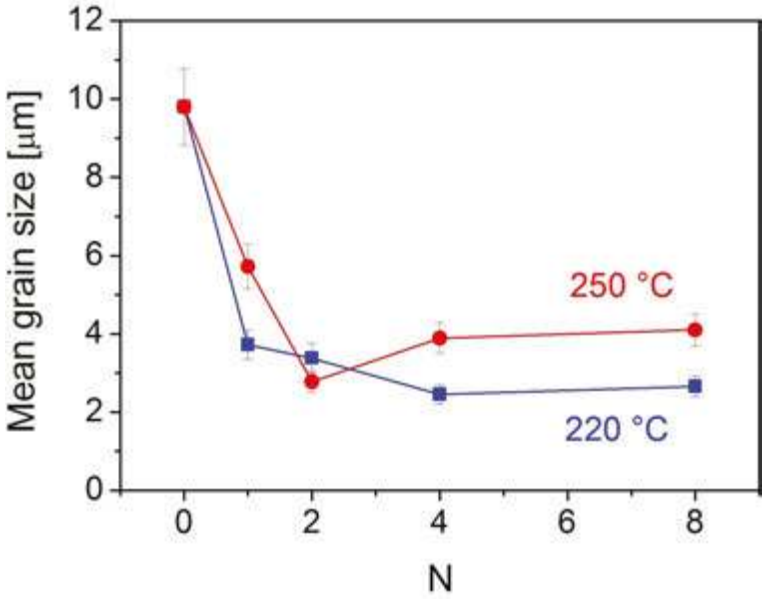

Figure 22. Evolution of the mean grain size on the processing temperature and number of ECAP passes.

techniques, especially for extrusion and rolling. Nevertheless, in the case of ECAP, the usual selection of alloys is usually limited to AZ, AM, and ZK types of alloys. The alloying elements in these types of alloys usually form stable secondary phases, or only small quantities of the atoms are dissolved in the Mg matrix. Therefore, the effect of the alloying elements on the deformation behaviour of the Mg matrix is highly limited. On the other hand, strong effect was observed in magnesium alloys containing lithium.

The effect of lithium on the final microstructure formed by ECAP in extruded AE42 (Mg, 4 wt%; Al, 2 wt% rare earths) and LAE442 (Mg, 4 wt%; Li, 4 wt%; Al, 2 wt% rare earths) magnesium alloys will be discussed in this section. The only difference between these two alloys is in the

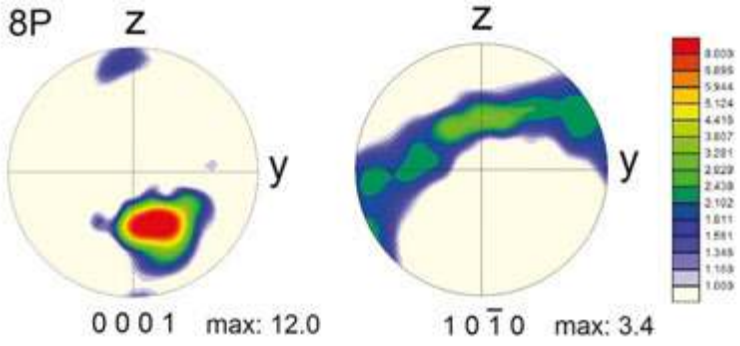

Figure 23. (0001) EBSD pole figure of the sample processed at 250°C (X-plane).

presence of lithium in the latter one. Lithium content in the alloy is below the solubility limit. It is very important as exceeding the solubility limit results in the formation of the mixture of HCP and BCC structure [59]. XRD measurement focused on the investigation of the effect of Li content on the lattice parameters of this alloy and showed a decrease of the *c*/*a* ratio to 1.610 [46], when compared to the pure Mg with *c*/*a* = 1.624 [60]. The decrease of the *c*/*a* ratio has a strong effect on the deformation behaviour as it facilitates the activation of non-basal slip systems.

The microstructure of both alloys was investigated by EBSD. Both alloys were processed by ECAP in the temperature range 180–220°C following route B_C up to 8 and 12P for AE42 and LAE442 alloys, respectively. The corresponding micrographs are shown in **Figure 24**. After the final step ECAP, the homogeneous microstructure with comparable grain size in both alloys of about ~1.5 μm was achieved. Effect of ECAP on grain refinement observed in both alloys is detailed elsewhere [55]. It should be noted that the reason for the processing by a higher number of passes of the LAE442 alloy was a much higher grain size in the initial condition. The effect of the grain size in the initial condition of the processed material on the effectivity of grain refinement was discussed in [61]. Our results are fully consistent with this work.

The microstructure of both alloys looks very similar. However, there is a significant difference in the texture, which has developed during ECAP processing. The corresponding pole figures are shown in **Figure 25**. The standard and usual texture was observed in both alloys after the extrusion [55]. The pole figure of the processed AE42 alloy is very similar to the texture observed in the AX41 alloy processed by ECAP (cf. **Figure 20**). On the other hand, the pole figure determined in the processed LAE442 alloy is completely different, even if the same processing conditions were employed. The pole figure contains a very strong M component, a weak N component and a new third component with basal planes perpendicular to the y-direction. The formation mechanism of the M and N components resulting from the predominant activation

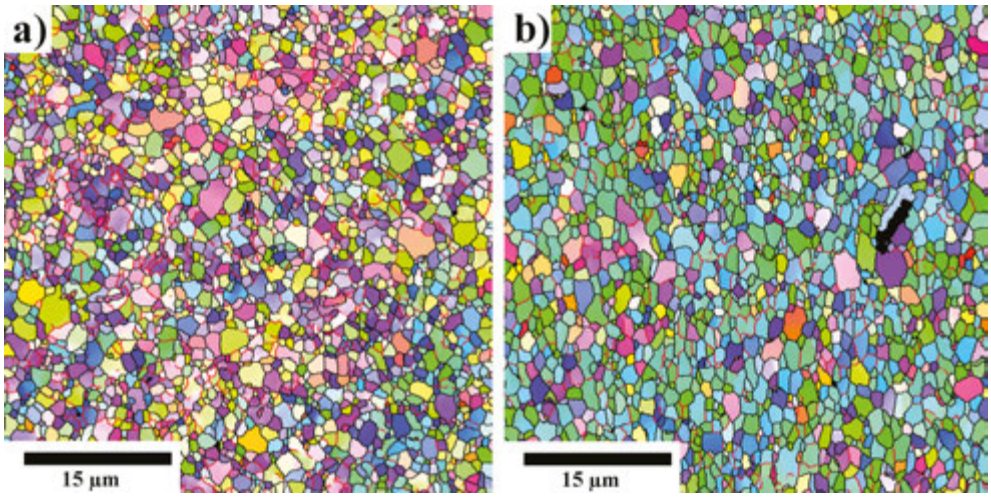

Figure 24. EBSD inverse pole figure maps of (a) AE42 and (b) LAE442 after the final step of ECAP.

http://dx.doi.org/10.5772/intechopen.68965

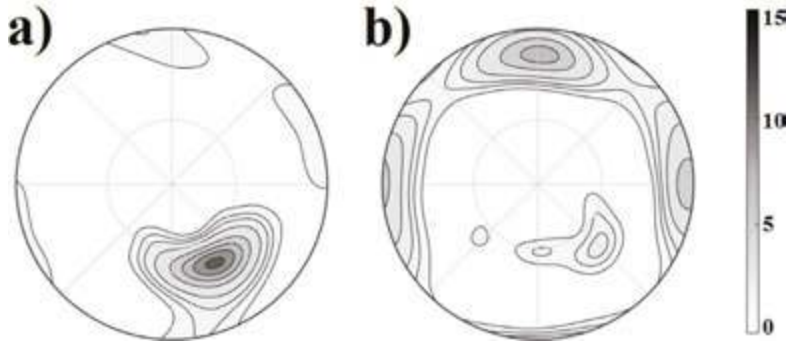

Figure 25. (0001) X-ray pole figure of (a) AE42 and (b) LAE442 after the final step of ECAP.

of the second-order pyramidal and basal slip, respectively, were discussed in Section 5.1. The new texture element, denoted as L, is associated with the activity of the prismatic slip system from the analysis of the $(10\bar{1}0)$ pole figure (see **Figure 26**). The main maximum is present on the z-axis and rotated by 15° from the processing direction. As described above and in Ref. [52], the rotation of the active slip planes parallel to the shear plane of the ECAP die causes the formation of the other texture element. Similarly, activation of the $\{(10\bar{1}0)\}\langle 11\bar{2}0\rangle$ prismatic slip system due to the lithium addition caused the rotation of the prismatic planes parallel to the shear plane of ECAP die as graphically expressed in **Figure 27**. Geometrically, this rotation causes the formation of the texture elements presented schematically in **Figure 26**.

5.4. Mechanical properties

In the previous section, it was shown that the microstructure of the processed magnesium alloy may be very different depending on the various processing parameters and the composition. Mechanical properties of the material are strongly affected by the microstructure, and therefore different evolution of the mechanical properties is expected. There are three

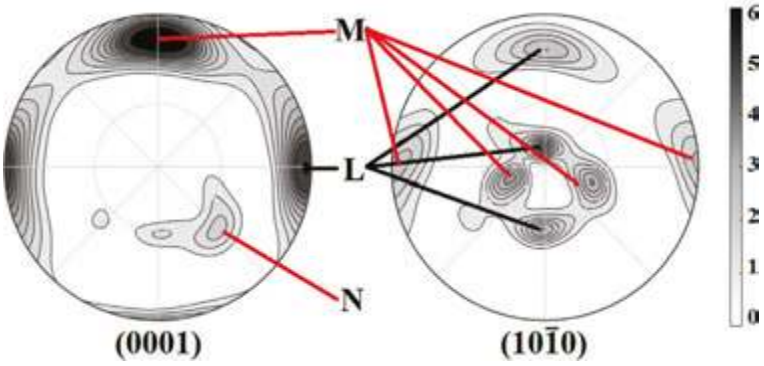

Figure 26. Depiction of the texture elements in the processed LAE442 alloy.

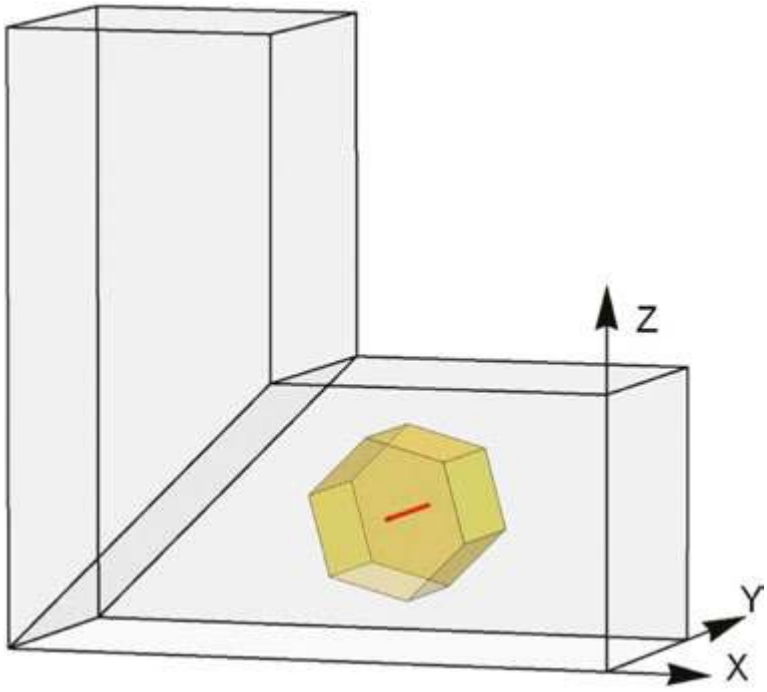

Figure 27. The formation mechanism of the texture component L.

main factors affecting the mechanical strength, namely, the grain size, the texture and the dislocation density. It is very hard to separate the effect of these individual parameters. However, the effect of the texture can be strongly suppressed by microhardness measurement, which simulates the multiaxial-loading. Therefore, it gives the opportunity to reveal the effect of grain refinement and hardening through dislocations. In **Figure 28(a)**, the dependence of the microhardness on the number of ECAP passes is shown. The microhardenss in individual samples increases with increasing number of ECAP passes and then saturates. The only exception is the AX41 sample processed via route C, in which the grain growth was observed. Grain boundary hardening is therefore an obvious source of the enhanced microhardness. Nevertheless, the possible effect of dislocations may also be assessed, when the data are evaluated considering the Hall-Petch relation. The highest difference in the discussed alloys was observed between AE42 and LAE442. **Figure 28(b)** shows the dependence of the microhardness on the square root of grain size for both alloys. The samples of the AE42 alloy obey the linear tendency of Hall-Petch relation, while in the LAE442 alloy, Hall-Petch relation is not met. The non-linear tendency and higher values of microhardness are the result of the increased dislocation density. **Figure 28(c)** shows the evolution of the dislocation density measured by PAS for both alloys. The evolution is very similar, but the values measured in the LAE442 alloy are by one order of magnitude higher than in the AE42 alloy. As a consequence, the effect of dislocations on the mechanical strength needs to be added to the calculation.

http://dx.doi.org/10.5772/intechopen.68965

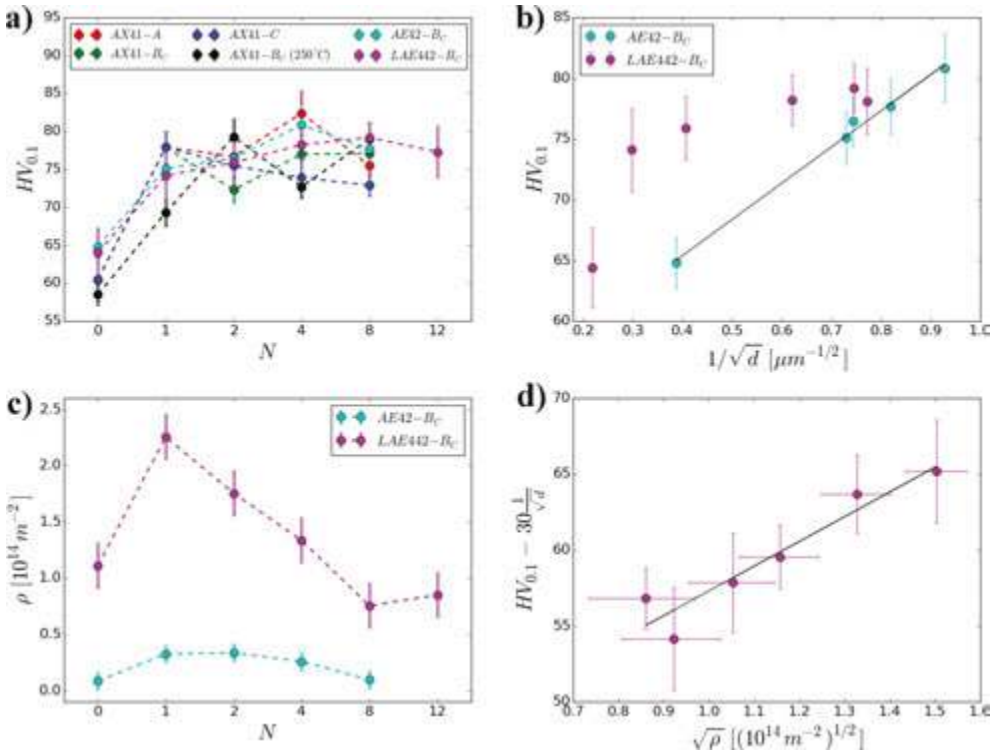

Figure 28. Evolution of microhardness in investigated Mg alloys. (a) The evolution of microhardnes different Mg alloys, (b) Hall-Petch relation for the AE42 and LAE442 alloys, (c) evolution of dislocation density in the AE42 and LAE442 alloys, (d) the evolution of reduced microhardness by grain boundary hardening as a function of square root of dislocation denisty in the LAE442 alloy.

Assuming that the grain boundary hardening is similar in both alloys (hardening coefficient was 30), it can be subtracted from the microhardenss and net effect of dislocations could be revealed. As shown in **Figure 28(d)**, the *HV* values corrected for the grain boundary hardening obey the linear relation when plotted vs. square root of the dislocation density. Variations of HV values of the AX41 alloy in **Figure 28(a)** are caused by variations of dislocation density. A detailed discussion of this effect is given elsewhere [45].

The evolution of the yield tensile strength shown in **Figure 29(a)** differs significantly from the evolution of the microhardness. The difference is caused by the mode of loading, i.e. by the change from multiaxial (microhardness) to an uniaxial loading (tensile tests), in which texture plays a significant role. The positive effect of the grain refinement and increased dislocation density on the mechanical stength can be overwhelmed by a negative effect of the texture that developes during ECAP. As shown above, strong texture is formed in investigated alloys regardeless of the processing route. Therefore, the strong anisotropy of the mechanical properties of the single crystal is transfered to the final material. The ECAP billet has ususally a form of a rod or a bar, and therefore the mechanical properties are ususally investigated in

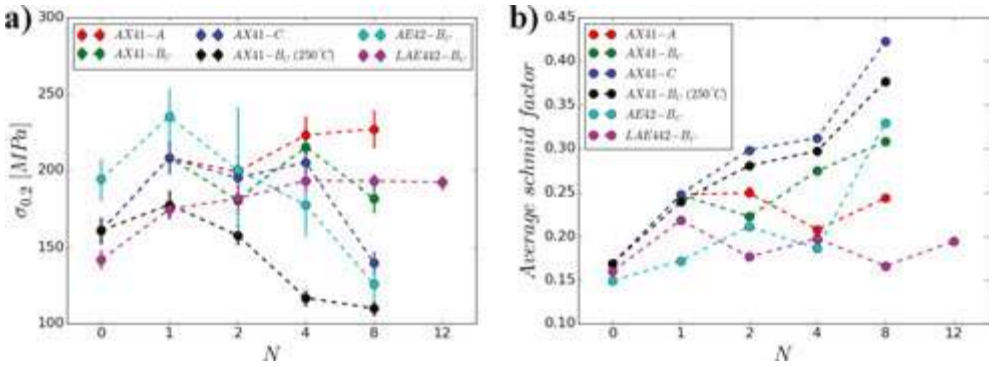

Figure 29. Mechanical properties of investigated Mg alloys. (a) The evolution of yield tenisle stress with strain, (b) the evolution of average Schmid factor calculated for uniaxial tension paralel to X-axis from EBSD data.

the direction paralel to the processing direction. Different evolution of mechanical proeprties was observed in individual samples even if the microstructure is strongly refined in all cases. As mentioned above, the reason is a strong texture formed in all samples, which differs in individual processing routes. The measure of the texture effect is the Schmid factor calculated for the basal slip (m_{basal}). Basal slip is the most favourable slip at room temperature, because its critical resolve shear stress is much lower than that of other slip systems. The plot of m_{basal} as a function of increasing number of ECAP pases is shown in **Figure 29(b)**. The strong correlation between m_{basal} and the tensile yield stress is clearly seen (cf. **Figure 29a** and **b**). The samples with higher value of m_{basal} exhibit lower yield stress. Deterioration of the yield tensile stress along the procesing direction is caused by the formation of the texture component N. Gradual reorientation of the grains by ~45° from the processing direction and also from the deformation axis facilitates the activation of the basal slip system, as manifested by enhanced values of m_{basal}. On the other hand, the formation of the strong texture component M in specimens processed by route A results in the same deterioration of mechanical properties when the deformation axis is rotated. As a consequence, the use of route A does not suppress the negative texture effect. The lowest anisotropy of mechanical properties was observed in the LAE442 alloy, where the final texture was not so sharp and all three texture components were present.

6. Conclusions

Microstructure and lattice defect evolution in ultrafine-grained materials of different crystal structure processed by ECAP have been investigated as a function of strain imposed to the material by severe plastic deformation and correlated with mechanical properties of these materials. The following conclusions may be drawn from this thorough study:

- ECAP proved to be an efficient technique of grain refinement. Ultrafine-grained materials of different crystal structure are obtained by this technique.
- The extent and the rate of the grain refinement strongly depend on the amount of the imposed strain and the parameters of ECAP processing.

- ECAP is more effective in FCC and BBC materials as compared to hexagonal materials. The difference is caused by different temperatures of processing and the concomitant processes occurring during pressing. Cubic materials may be processed at room temperature while elevated temperatures are needed to process HPC materials.
- In HCP materials, the dynamic recrystallization is the most effective refinement mechanism, while in BCC and FCC materials a dominant mechanism of grain refinement is controlled by the gradual transformation of LAGBs to HAGBs.
- ECAP-processed materials exhibit strong a crystallographic texture, which depends on the chemical composition, the temperature and the processing route.
- A high density of lattice defects was found in severely deformed material processed by ECAP. Significantly higher density of dislocations was found in materials with cubic structure than in hexagonal materials (by at least one order of magnitude). FCC metals also contain a high concentration of vacancies and their conglomerates called microvoids while in BCC and hexagonal materials vacancy concentration is very low (below the detection limit of PAS).
- Positron annihilation spectroscopy and X-ray diffraction proved to be efficient and complementary techniques of the determination of the dislocation density over a wide range of orders of magnitudes.
- Processing of materials having FCC and BCC lattice leads to the enhanced strength, which is accompanied by reduced ductility.
- Improved strength of UFG materials is caused by a combination of strong grain refinement and increased dislocation density.
- Mechanical properties in HCP materials are significantly affected by the grain size, dislocation density and texture, which results in their strong anisotropy.

Acknowledgements

This work was financially supported by the Czech Science Foundation under the project GB 14-36566G and by ERDF under the project 'Nanomaterials centre for advanced applications', project No. CZ.02.1.01/0.0/0.0/15_003/0000485.

Author details

Peter Minárik[1], Tomáš Krajňák[1], Ondřej Srba[2], Jakub Čížek[1], Jenő Gubicza[3], Milan Dopita[1], Radomír Kužel[1] and Miloš Janeček[1]*

*Address all correspondence to: janecek@met.mff.cuni.cz

1 Charles University, Prague, Czech Republic

2 Research Center Rez, Czech Republic

3 L. Eotvos Unviersity, Budapest, Hungary

References

[1] Sabirov I, Enikeev NA, Murashkin MY, Valiev RZ. Bulk Nanostructured Materials with Multifunctional Properties. Berlin/Heidelberg: Springer; 2015. p. 125

[2] Iwahashi Y, Horita Z, Nemoto M, Langdon TG. Factors influencing the equilibrium grain size in equal-channel angular pressing: Role of Mg additions to aluminum. Metallurgical and Materials Transactions A. 1998;**29**(10):2503-2510

[3] Nakashima K, Horita Z, Nemoto M, Langdon TG. Development of a multi-pass facility for equal-channel angular pressing to high total strains. Materials Science and Engineering: A. 2000;**281**(1-2):82-87

[4] Raab GJ, Valiev RZ, Lowe TC, Zhu YT. Continuous processing of ultrafine grained Al by ECAP–Conform. Materials Science and Engineering: A. 2004;**382**(1-2):30-34

[5] West RN. Positron studies of lattice defects in metals. In: Hautojärvi PDP, editor. Positrons in Solids. Berlin/Heidelberg: Springer; 1979. pp. 89-144 (Topics in Current Physics)

[6] Oberdorfer B, Würschum R. Positron trapping model for point defects and grain boundaries in polycrystalline materials. Physical Review B. 2009;**79**(18):184103

[7] Čížek J, Procházka I, Cieslar M, Kužel R, Kuriplach J, Chmelík F, et al. Thermal stability of ultrafine grained copper. Physical Review B. 2002;**65**(9):094106

[8] Ribárik G, Gubicza J, Ungár T. Correlation between strength and microstructure of ball-milled Al–Mg alloys determined by X-ray diffraction. Materials Science and Engineering: A. 2004;**387-389**:343-347

[9] Máthis K, Nyilas K, Axt A, Dragomir-Cernatescu I, Ungár T, Lukáč P. The evolution of non-basal dislocations as a function of deformation temperature in pure magnesium determined by X-ray diffraction. Acta Materialia. 2004;**52**(10):2889-2894

[10] Williams DB, Carter CB. Transmission Electron Microscopy: A Textbook for Materials Science. 2nd ed. New York: Springer; 2009. p. 820

[11] Schwartz AJ, Kumar M, Field DP, Adams BL, editors. Electron Backscatter Diffraction in Materials Science. 1st ed. New York: Springer; 2000. p. 350

[12] Furukawa M, Iwahashi Y, Horita Z, Nemoto M, Langdon TG. The shearing characteristics associated with equal-channel angular pressing. Materials Science and Engineering: A. 1998;**257**(2):328-332

[13] Dalla Torre F, Lapovok R, Sandlin J, Thomson PF, Davies CHJ, Pereloma EV. Microstructures and properties of copper processed by equal channel angular extrusion for 1-16 passes. Acta Materialia. 2004;**52**(16):4819-4832

[14] Janeček M, Hadzima B, Hellmig RJ, Estrin Y. The influence of microstructure on the corrosion properties of cu polycrystals prepared by ecap. Kov Materiály. 2005;**43**(4):258-271

[15] Dopita M, Janeček M, Rafaja D, Uhlíř J, Matěj Z, Kužel R. EBSD investigation of the grain boundary distributions in ultrafine-grained Cu and Cu–Zr polycrystals prepared by equal-channel angular pressing. International Journal of Materials Research. 2009;**100**(6):785-789

[16] Christian JW, Mahajan S. Deformation twinning. Progress in Materials Science. 1995;**39**(1):1-157

[17] Huang CX, Wang K, Wu SD, Zhang ZF, Li GY, Li SX. Deformation twinning in polycrystalline copper at room temperature and low strain rate. Acta Materialia. 2006;**54**(3):655665

[18] McKee BTA, Saimoto S, Stewart AT, Stott MJ. Positron trapping at dislocations in copper. Canadian Journal of Physics. 1974;**52**(9):759-765

[19] Barbiellini B, Puska MJ, Torsti T, Nieminen RM. Gradient correction for positron states in solids. Physical Review B. 1995;**51**(11):7341-7344

[20] Ribárik G, Ungár T, Gubicza J. MWP-fit: A program for multiple whole-profile fitting of diffraction peak profiles by ab initio theoretical functions. Journal of Applied Crystallography. 2001;**34**(5):669-676

[21] Matěj Z, Nichtová L, Kužel R. Expanding FOX for microstructural analysis. Materials and Structures. **15**(1)

[22] Gubicza J, Nam NH, Balogh L, Hellmig RJ, Stolyarov VV, Estrin Y, et al. Microstructure of severely deformed metals determined by X-ray peak profile analysis. Journal of Alloys and Compounds. 2004;**378**(1-2):248-252

[23] Caillard D. Kinetics of dislocations in pure Fe. Part I. In situ straining experiments at room temperature. Acta Materialia. 2010;**58**(9):3493-3503

[24] Ungár T, Tichy G, Gubicza J, Hellmig RJ. Correlation between subgrains and coherently scattering domains. Powder Diffraction. 2005;**20**(4):366-375

[25] Kuzel R, Cherkaska V, Matej Z, Janecek M, Cizek J, Dopita M. Structural studies of submicrocrystalline copper and copper composites by different methods. Zeitschrift für Kristallographie Supplements. 2008;**27**:73-80

[26] Máthis K, Krajnák T, Janeček M, Dopita M, Kim HS. Microstructural evolution of equal-channel angular pressed interstitial-free steel. International Journal of Materials Research. 2009;**100**(6):834-837

[27] Máthis K, Krajňák T, Kužel R, Gubicza J. Structure and mechanical behaviour of interstitial-free steel processed by equal-channel angular pressing. Journal of Alloys and Compounds. 2011;**509**(8):3522-3525

[28] Čížek J, Janeček M, Krajňák T, Stráská J, Hruška P, Gubicza J, et al. Structural characterization of ultrafine-grained interstitial-free steel prepared by severe plastic deformation. Acta Materialia. 2016;**105**:258-272

[29] Langdon TG. The principles of grain refinement in equal-channel angular pressing. Materials Science and Engineering: A. 2007;**462**(1-2):3-11

[30] Xu C, Furukawa M, Horita Z, Langdon TG. The evolution of homogeneity and grain refinement during equal-channel angular pressing: A model for grain refinement in ECAP. Materials Science and Engineering: A. 2005;**398**(1-2):66-76

[31] Valiev RZ, Langdon TG. Principles of equal-channel angular pressing as a processing tool for grain refinement. Progress in Materials Science. 2006;**51**(7):881-981

[32] Shin DH, Kim W-J, Choo WY. Grain refinement of a commercial 0.15%C steel by equal-channel angular pressing. Scripta Materialia. 1999;**41**(3):259-262

[33] Bozorth RM. The orientations of crystals in electrodeposited metals. Physical Review. 1925;**26**(3):390-400

[34] De Messemaeker J, Verlinden B, Van Humbeeck J. Texture of IF steel after equal channel angular pressing (ECAP). Acta Materialia. 2005;**53**(15):4245-4257

[35] Baczynski J, Jonas JJ. Texture development during the torsion testing of α-iron and two IF steels. Acta Materialia. 1996;**44**(11):4273-4288

[36] Toth LS, Jonas JJ, Daniel D, Bailey JA. Texture development and length changes in copper bars subjected to free end torsion. Texture Stress Microstructure. 1992;**19**(4):245-262

[37] Montheillet F, Cohen M, Jonas JJ. Axial stresses and texture development during the torsion testing of Al, Cu and α-Fe. Acta Materialia. 1984;**32**(11):2077-2089

[38] Park Y-K, Waber JT, Meshii M, Snead CL, Park CG. Dislocation studies on deformed single crystals of high-purity iron using positron annihilation: Determination of dislocation densities. Physical Review B. 1986;**34**(2):823-836

[39] Čížek J, Procházka I, Kočík J, Keilová E. Positron lifetime study of reactor pressure vessel steels. Physica Status Solidi A. 2000;**178**(2):651-662

[40] Hidalgo C, González-Doncel G, Linderoth S, San Juan J. Structure of dislocations in Al and Fe as studied by positron-annihilation spectroscopy. Physical Review B. 1992;**45**(13):7017-7021

[41] Ngan AHW, Wen M. Atomistic simulation of energetics of motion of screw dislocations in bcc Fe at finite temperatures. Computational Materials Science. 2002;**23**(1-4):139-145

[42] Mckenzie PWJ, Lapovok R. ECAP with back pressure for optimum strength and ductility in aluminium alloy 6016. Part 2: Mechanical properties and texture. Acta Materialia. 2010;**58**(9):3212-3222

[43] Kim HS, Ryu WS, Janecek M, Baik SC, Estrin Y. Effect of equal channel angular pressing on microstructure and mechanical properties of IF steel. Advanced Engineering Materials. 2005;**7**(1-2):43-46

[44] Duan Y, Tang L, Xu G, Deng Y, Yin Z. Microstructure and mechanical properties of 7005 aluminum alloy processed by room temperature ECAP and subsequent annealing. Journal of Alloys and Compounds. 2016;**664**:518-529

[45] Krajňák T, Minárik P, Gubicza J, Máthis K, Kužel R, Janeček M. Influence of equal channel angular pressing routes on texture, microstructure and mechanical properties of extruded AX41 magnesium alloy. Materials Characterization. 2017;**123**:282-293

[46] Minárik P, Král R, Pešička J, Daniš S, Janeček M. Microstructure characterization of LAE442 magnesium alloy processed by extrusion and ECAP. Materials Characterization. 2016;**112**:1-10

[47] Li S. Orientation stability in equal channel angular extrusion. Part II: Hexagonal close-packed materials. Acta Materialia. 2008;**56**(5):1031-1043

[48] Agnew SR, Mehrotra P, Lillo TM, Stoica GM, Liaw PK. Texture evolution of five wrought magnesium alloys during route A equal channel angular extrusion: Experiments and simulations. Acta Materialia. 2005;**53**(11):3135-3146

[49] Lin HK, Huang JC, Langdon TG. Relationship between texture and low temperature superplasticity in an extruded AZ31 Mg alloy processed by ECAP. Materials Science and Engineering: A. 2005;**402**(1-2):250-257

[50] Janeček M, Yi S, Král R, Vrátná J, Kainer KU. Texture and microstructure evolution in ultrafine-grained AZ31 processed by EX-ECAP. Journal of Materials Science. 2010;**45**(17):4665-4671

[51] Kim WJ, An CW, Kim YS, Hong SI. Mechanical properties and microstructures of an AZ61 Mg Alloy produced by equal channel angular pressing. Scripta Materialia. 2002;**47**(1):39-44

[52] Agnew SR, Horton JA, Lillo TM, Brown DW. Enhanced ductility in strongly textured magnesium produced by equal channel angular processing. Scripta Materialia. 2004;**50**(3):377-381

[53] Kim WJ, Hong SI, Kim YS, Min SH, Jeong HT, Lee JD. Texture development and its effect on mechanical properties of an AZ61 Mg alloy fabricated by equal channel angular pressing. Acta Materialia. 2003;**51**(11):3293-3307

[54] Liu T, Wang YD, Wu SD, Lin Peng R, Huang CX, Jiang CB, et al. Textures and mechanical behavior of Mg–3.3%Li alloy after ECAP. Scripta Materialia. 2004;**51**(11):1057-1061

[55] Minárik P, Král R, Čížek J, Chmelík F. Effect of different c/a ratio on the microstructure and mechanical properties in magnesium alloys processed by ECAP. Acta Materialia. 2016;**107**:83-95

[56] Yin SM, Wang CH, Diao YD, Wu SD, Li SX. Influence of grain size and texture on the yield asymmetry of Mg-3Al-1Zn alloy. Journal of Materials Science & Technology. 2011;**27**(1):29-34

[57] E. Sukedai TY. Investigation of tensile–compressive yield asymmetry and the role of deformation twin in extruded pure magnesium. International Journal of Materials Research. 2010;**101**(6):736-740

[58] Langdon TG. Twenty-five years of ultrafine-grained materials: Achieving exceptional properties through grain refinement. Acta Materialia. 2013;**61**(19):70357059

[59] Massalski TB, Okamoto H. Binary Alloy Phase Diagrams. 2nd ed. Materials Park, OH: The Materials Information Society; 1990

[60] Pekguleryuz M, Kainer K, Kaya A. Fundamentals of Magnesium Alloy Metallurgy. Elsevier; 2013. p. 381

[61] Figueiredo RB, Langdon TG. Principles of grain refinement in magnesium alloys processed by equal-channel angular pressing. Journal of Materials Science. 2009;**44**(17): 4758-4762